*Progress In Electromagnetics Research, PIER 18, 67–83, 1998*

# EXTENSION OF THE CLEAN TECHNIQUE TO THE MICROWAVE IMAGING OF CONTINUOUS THERMAL SOURCES BY MEANS OF APERTURE SYNTHESIS RADIOMETERS

A. Camps, J. Bará, F. Torres, and I. Corbella

Universitat Politècnica de Catalunya
Dept. of Signal Theory and Communications
c/Gran Capità s/n, 08034 Barcelona, Spain



## 1. INTRODUCTION

Interferometric radiometers measure the correlation between the analytic narrow-band random signals $b_k(t)$ and $b_l(t)$ collected by the $(k,l)$ pair of antennas of a sparse array. Each correlation is a sample of the so called visibility function $V(u,v)$ (units of Kelvin)

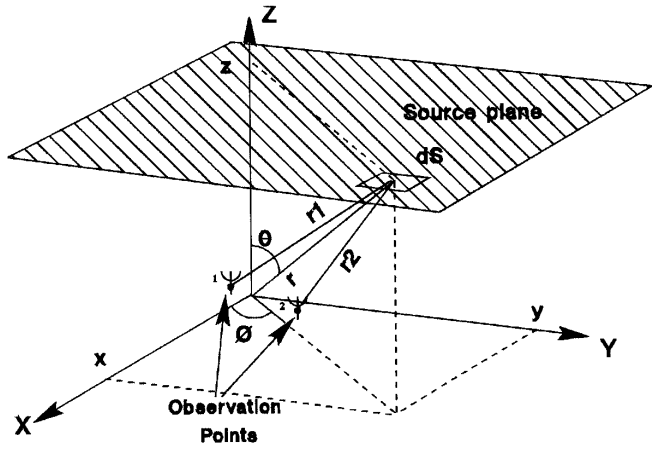


**Figure 1.** Interferometer geometry and definition of magnitudes.

$$
\begin{aligned}
V_{kl}(u_{kl}, v_{kl}) =& \frac{1}{2} E[b_k(t) b_l^*(t)] \\
=& \iint_{\xi^2+\eta^2 \le 1} \frac{T_B(\xi,\eta)}{\sqrt{1-\xi^2-\eta^2}} F_{n_k}(\xi,\eta) F_{n_l}^*(\xi,\eta) \\
& \tilde{r}_{kl}\left(-\frac{u_{kl}\xi + v_{kl}\eta}{f_0}\right) e^{-j2\pi(u_{kl}\xi + v_{kl}\eta)} d\xi d\eta
\end{aligned}
\tag{1}
$$

where: $(u_{kl}, v_{kl}) = (x_l - x_k, y_l - y_k)/\lambda$ is the normalized spacing between the antennas (Figure 1)

$E[\ ]$ is the expected value operator.

$(\xi, \eta) = (\sin\theta\cos\phi, \sin\theta\sin\phi)$ are the direction cosines with respect X and Y (Figure 1)

$T_B(\xi, \eta)$ is the brightness temperature (units of Kelvin)

$F_{n_{k,l}}(\xi, \eta)$ is the normalized antenna voltage pattern (without units) of the antennas $k$ and $l$.

$\tilde{r}_{kl}(t) = r_{kl}(t) e^{-j2\pi f_0 t}$ is the so called fringe-wash function, which accounts for spatial decorrelation effects

$$
r_{kl}(t) = \int_0^\infty H_{nk}(f) H_{nl}^*(f) e^{j2\pi f t} df \tag{2}
$$

where $H_{n\ k,l}(f)$ is the normalized frequency response of receivers $k$ and $l$, and $f_0$ is their center frequency. In the limiting narrow-band case, decorrelation effects are negligible and $\tilde{r}_{kl} \approx 1$.

For an ideal interferometer having identical receivers and antennas, and negligible decorrelation effects $\tilde{r}(t) \approx 1$, the visibility function and the brightness temperature are related by a Fourier transform

$$V(u,v) \overset{\mathcal{F}}{\longleftrightarrow} \breve{T}(\xi,\eta) \triangleq \frac{T_B(\xi,\eta)}{\sqrt{1-\xi^2-\eta^2}} |F_n(\xi,\eta)|^2 \tag{3}$$

In the spatial domain, $\breve{T}(\xi,\eta)$ is a function supported by the unit circle $\xi^2+\eta^2 \leq 1$. In [1–3] it is shown that the optimum sampling strategy in the $(u,v)$ domain is the hexagonal one, for a determined alias free field of view (FOV). Hexagonal $(u,v)$ sampling provides a reduction of a 13.4% of the required visibility samples and the associated hardware, with respect to rectangular sampling. This kind of sampling is achieved by, i.e., Y-shaped arrays, which are the ones that provide the largest $(u,v)$ coverage and the best angular resolution [4, 5]. In [3] it is shown that standard rectangular FFT routines can be directly applied to process hexagonally sampled signals provided that the pixels on the $(\xi,\eta)$ domain are chosen over the reciprocal hexagonal grid of the $(u,v)$ hexagonal grid. This fact is of great importance since it avoids interpolations that may induce artifacts in the recovered image. It also preserves signal-to-noise ratio and increases the computational speed.

When there are antenna position errors, and mismatches between antenna voltage pattems and receivers' frequency responses, the inversion of Equation 1 has not an analytic solution. Iterative techniques are then required, which are the object of this paper.

## 2. THE CLEAN TECHNIQUE

A solution to the inversion of Equation 1 is provided by the CLEAN algorithm, devised by Hogbom in 1974 [6] for non-coherent radiation fields generated by independent point sources, such as stars. The starting point of the standard CLEAN algorithm is the so called dirty image $\hat{T}(\xi,\eta)$, obtained from the inverse Fourier transform of Equation 1

$$\hat{T}(\xi,\eta) = F^{-1}[V(u,v)] = \iint_{\xi'^2+\eta'^2\leq 1} AF(\xi,\xi',\eta,\eta') T(\xi',\eta') d\xi' d\eta' \tag{4}$$

where $T(\xi,\eta) = T_B(\xi,\eta)/\sqrt{1-\xi^2-\eta^2}$ and the equivalent array factor $AF(\xi,\xi',\eta,\eta')$, also called dirty beam, is defined as the space-variant impulse response at $(\xi,\eta)$ to a point source located at $(\xi',\eta')$.

For the hexagonal $(u, v)$ sampling it is given by

$$AF(\xi, \xi', \eta, \eta') = \frac{\sqrt{3}d^2}{2} \sum_{k=1}^{N_T} \sum_{l=1}^{N_T} W(u_{kl}, v_{kl}) F_{n_k}(\xi', \eta') F_{n_l}^*(\xi', \eta') \tilde{r}_{kl} \left( -\frac{u_{kl}\xi' + v_{kl}\eta'}{f_0} \right) e^{j2\pi[u_{kl}(\xi - \xi') + v_{kl}(\eta - \eta')]} \quad (5)$$

where $N_T$ is the total number of antennas of the Y-array [3], and $W(u_{kl}, v_{kl})$ is a weighing function used to taper the visibility samples to reduce side lobes. A very smooth function such as the standard Blackmann window, with rotational symmetry, is usually used to reduce side lobes, at the expense of a poorer angular resolution [4]. The standard CLEAN algorithm represents a radio source $T(\xi, \eta)$ by a number of point sources -stars- in an empty FOV. An iterative approach is employed to find the positions and strengths of these point sources:

i) At each iteration, the position $(\xi', \eta')$ and the strength of the most brilliant (absolute value) peak is found in the dirty image $\hat{T}(\xi, \eta)$ (Equation 4). In some cases it is interesting to search only in a restricted area, as it will become apparent in the next section.

ii) The dirty beam centered at the point $(\xi', \eta')$, $AF(\xi, \xi', \eta, \eta')$ (Equation 5), is subtracted from the dirty image $\hat{T}(\xi', \eta')$ multiplied by the peak strength and a damping factor, usually in the range [0.1, 0.25]. Note that this process subtracts not only the main lobe of $AF$, but also the side lobes that are responsible of most of the artifacts in the dirty image.

iii) The process is repeated until any remaining peak is below an specified threshold.

Finally, the "cleaned" image is found as the sum of a set of point sources at the positions where they were detected with their corresponding strength. The "cleaned" image is finally convolved with a beam, usually a Gaussian one -without secondary lobes-, with the same half-power beam-width as $AF$. This process low-pass filters the high frequency components that have been extrapolated, which are usually very noisy. More sophisticated versions of the standard CLEAN algorithm, such as the Clark or the Cotton-Schwab algorithms [7, 8], can be found in the literature.

From its principles it is clear that, in this form, the CLEAN algorithm is very well suited to recover quasi-point sources. However, it must be extended to the Earth observation case, in which the Earth appears as an extended thermal source filling almost completely the FOV.

## 3.EXTENSION OF THE CLEAN TECHNIQUE TO THE MICROWAVE IMAGING OF EXTENDED THERMAL SOURCES

This section describes a proposed inversion algorithm suitable to large two-dimensional interferometric radiometers devoted to Earth observation. It is supposed that receiver errors and antenna coupling errors are calibrated by other means [9, 10]. Hence, the visibility samples used by the algorithm are mainly corrupted by antenna voltage pattem mismatches and antenna position errors, which must be accurately measured.

### 3.1 The use of "a priori" information: The processing of differential visibililies

In order to avoid conditions that cannot be met in a real situation, only the following "a priori" information is used: i) the average sky brightness temperature $T_{sky} \approx 2.7$ K at 1.4 GHz — provided that neither the sun, the moon, the center of the galaxy or any other radiation source enters directly in the antenna beam or by a reflection over the Earth-, and ii) the Earth-sky horizon as seen from the satellite at a given altitude with a given tilt angle (Equation 10, Figure 2). With this data, the set of visibility samples to be processed can be expressed as

$$\Delta V(u,v) = V(u,v) - T_{SKY}V_{SKY}(u,v) - T_{EARTH}V_{EARTH}(u,v) \quad (6)$$

where $V_{SKY}(u,v)$ and $V_{EARTH}(u,v)$ are the contributions from the Sky, and for a uniform brightness temperature Earth. $V_{SKY}(u,v)$ and $V_{EARTH}(u,v)$ are computed from Equation 1, which includes the information of antenna voltage patterns $F_{n\ k,l}(\xi,\eta)$, antenna positions $(u_{kl},v_{kl}) = (x_l - x_k, y_l - y_k)/\lambda$ and receiver frequency responses (Equation 2).

$$V_{SKY(k,l)}(u_{kl},v_{kl}) \triangleq \iint_{\xi^2+\eta^2\leq 1-earth(\xi,\eta)} F_{n_k}(\xi,\eta)F^*_{n_l}(\xi,\eta) \tilde{r}_{kl}\left(-\frac{u_{kl}\xi+v_{kl}\eta}{f_0}\right)e^{-j2\pi(u_{kl}\xi+v_{kl}\eta)}d\xi d\eta \quad (7)$$

$$V_{EARTH(k,l)}(u_{kl},v_{kl}) \triangleq \iint_{earth(\xi,\eta)} F_{n_k}(\xi,\eta)F^*_{n_l}(\xi,\eta) \tilde{r}_{kl}\left(-\frac{u_{kl}\xi+v_{kl}\eta}{f_0}\right)e^{-j2\pi(u_{kl}\xi+v_{kl}\eta)}d\xi d\eta \quad (8)$$

Note that $V_{SKY}(u,v)$ and $V_{EARTH}(u,v)$ are normalized visibilities (without units), while $V(u,v)$ and $\Delta V(u,v)$ have the units of Kelvin. The value of $T_{EARTH}$ is selected to force that $\Delta V(0,0)=0$ in Equation 6, that is, its inverse Fourier transform is a zero mean function.

$$T_{EARTH} \triangleq \frac{V(0,0)-T_{SKY}\iint_{\xi^2+\eta^2\leq 1-earth(\xi,\eta)}|F_{n_0}(\xi,\eta)|^2 d\xi d\eta}{\iint_{earth(\xi,\eta)}|F_{n_0}(\xi,\eta)|^2 d\xi d\eta} \quad (9)$$

In Equations 7, 8 and 9, the Earth-Sky horizon is defined by [3]

$$earth(\xi,\eta)=\begin{cases}1 & \text{for } \left(\frac{\xi}{a}\right)^2+\left(\frac{\eta+\eta_0}{b}\right)^2\leq 1,\\ 0 & \text{elsewhere}\end{cases} \quad (10)$$

with $a=0.888$, $b=0.760$ and $\eta_0=0.234$, for a 790 Km height orbit with a tilt angle of $\beta=31.2^\circ$ with respect to nadir. The function $|F_{n_0}(\xi,\eta)|^2$ in Equation 9 stands for the radiation pattern of the radiometer antenna that measures the antenna temperature $V(0,0)$. In the MIRAS case, an extra antenna, named 0, is devoted to this purpose.

$T_B(\xi,\eta)$ in Equation 1 will be recovered now from its average value $T_{EARTH}$ and the deviations from the mean value given the differential visibilities $\Delta V(u,v)$ (Equation 6). It is important to point out two important features of the proposed algorithm: i) the alias free FOV (Figure 2) is expanded by removing the sky brightness temperature, and it is now limited by the periodic repetition of the Earth-sky horizon, not by the periodic repetition of the unit circle. ii) on the other hand, by removing the average value of the brightness temperature of

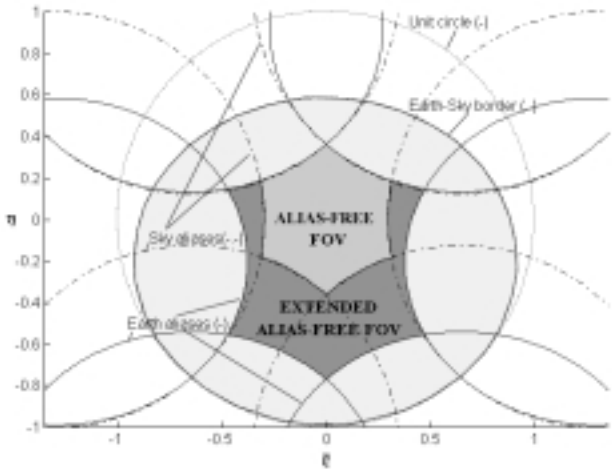


**Figure 2.** Earth and Sky contours, Earth and Sky aliases and Alias-Free Field of View.

the Earth, $T_{EARTH}$ the error introduced by the Gibbs phenomenon of the six Earth aliases is significantly reduced.

### 3.2 Description of the proposed method

The proposed algorithm proceeds in a similar way as the "CLEAN" algorithm does, with the following differences:

i) The inversion must be limited to the extended alias free FOV (Figure 2), since the brightness temperature can not be recovered in regions where two or even three pixels are overlapping. A guard-pixel is left at the border of the alias free FOV to minimize the errors introduced by the truncation of the tails of the equivalent array factors (Equation 5) of pixels lying in the aliased zone that enter in the alias free FOV and vice-versa.

ii) on the other hand, since the thermal source is continuous, the direct application of the search method used in the standard CLEAN (step (i), section 2) leads to bumpy brightness temperature maps. To overcome this problem, all the pixels lying in the alias free FOV are "cleaned" simultaneously at each iteration (Equations 14–15).

Once the contributions of the Sky and a constant brightness temperature Earth have been removed from $V(u,v)$, Equation 1 is solved for the differential visibilities $\Delta V(u,v)$ (Equation 6) discretized according the $(u,v)$ sampling grid and its $(\xi,\eta)$ reciprocal one [3, 4]

$$\Delta T^{raw}(\xi,\eta) = F_H^{-1}[W(u,v)\Delta V(u,v)]./\left|\overline{F_n(\xi,\eta)}\right|^2 \tag{11}$$

where $\Delta T^{raw}(\xi,\eta)$ corresponds to the discretization of the approximated brightness temperature map $\hat{T}(\xi,\eta) - T_{EARTH}$ (Equation 4) truncated to the alias free FOV and compensated by the average antenna radiation pattern $\left|\overline{F_n(\xi,\eta)}\right|^2$ of all the antennas

$$\left|\overline{F_n(\xi,\eta)}\right|^2 \triangleq \frac{1}{N}\sum_{k=1}^{N_T}|F_{n_k}(\xi,\eta)|^2 \tag{12}$$

the $F_H^{-1}$ operator stands for the hexagonal inverse Fourier Transform operator [3] and the '$./$' operator stands for the division element by element. Equation 1 stablishes a linear relationship between the measured differential visibility samples $\Delta V(u,v)$ and the differential temperatures $\Delta T^{dec}(\xi,\eta)$, the solution that we are looking for. This relationship can be written as

$$\Delta V(u,v) = G[\Delta T^{dec}(\xi,\eta)] \tag{13}$$

where the $G$ operator is the integral operator that generates the set of visibility samples from a given brightness temperature map, according to the known antenna radiation voltage patterns, antenna positions and receivers' frequency responses (Equation 1). It should be pointed out that the $G$ defined by Equation 13 does not correspond to the one used in [11, 12] which includes antenna coupling effects, etc. With this notation, Equation 11 can be rewritten in the form

$$\Delta T^{raw}(\xi,\eta) = F_H^{-1}[G[\Delta T^{dec}(\xi,\eta)]]./\left|\overline{F_n(\xi,\eta)}\right|^2 \triangleq H[\Delta T^{dec}(\xi,\eta)] \tag{14}$$

$$H[x(\xi,\eta)] \triangleq F_H^{-1}[G[x(\xi,\eta)]]./\left|\overline{F_n(\xi,\eta)}\right|^2$$

where the $H$ operator is the system's impulse response, that is, the $AF$ of each pixel (Equation 5) compensated by the average antenna radiation pattem (Equation 12).

lt has been found that the formulation of the problem over the modified temperatures (Equation 11) rather than over the visibility samples (Equation 1) is advantageous because aliasing effects are more easily removed in the $(\xi, \eta)$ domain. Note also that the operator $F_H^{-1}\{\ \}./\left|\overline{F}_n\right|^2$ acts as a pre-conditioner of the $G$ operator, as used in some Conjugate Gradient algorithms to improve the speed of convergence [12]. In fact, in the ideal case, when all the antenna patterns are identical and fringe-washing effects are negligible $G^{-1} = F_H^{-1}\{\ \}./\left|\overline{F}_n\right|^2$, the $H$ operator becomes the identity operator, and the process stops at the first iteration. In a general case, the speed of convergence of the method depends on the eigenvalues of the $H$ operator, which can be improved by selecting an appropriate damping factor (appendix 1).

The inversion method proceeds as follows

i) Iterations are started for $k = 1, 2, 3, \ldots$

$$\Delta T^{res(k+1)} = (I - H)\Delta T^{res(k)} = (I - H)^{(k+1)}\Delta T^{raw} \to 0 \tag{15}$$

$$\Delta T^{dec(k+1)} = \Delta T^{dec(k)} + \Delta T^{res(k)} = \sum_{n=0}^{k}(I - H)^n \Delta T^{raw} \to H^{-1}\Delta T^{raw} \tag{16}$$

with the initial values

$$\Delta T^{res(1)} = (I - H)\Delta T^{raw} \tag{17}$$

and

$$\Delta T^{dec(1)} = \Delta T^{raw} \tag{18}$$

where $\Delta T^{raw}$ is given by Equation 11, and both $\Delta T^{res(k)}$ and $\Delta T^{dec(k)}$ are truncated to the extended alias-free FOV.

ii) Step (i) is repeated until the squared Euclidean norm of the residue decreases below a determined threshold

$$\left\| \left|\overline{F}_n\right|^2 \Delta T^{res(k)} \right\|_2^2 \leq \Delta T^2 = \Delta T_{noise}^2 + \Delta T_{Gibbs}^2 \tag{19}$$

The first term on the right hand side of Equation 19 corresponds to the thermal noise contribution to the raw brightness temperature and can be computed with the formulas derived in [7, 8, 11, 12, 14]. The second one corresponds to the ringing due to the limited $(u, v)$

coverage (Gibbs phenomenon) and depends basically on the value of the average brightness temperature of the Earth, $T_{EARTH}$ (Equation 9), and the window used to taper the visibility samples [4, 5].

In fact, the $H$ operator can be easily evaluated (Equation 14) by computing the intermediate visibilities multiplying, row by row, the $G$ operator by the modified temperature distribution, taking the two-dimensional inverse Fourier transform over the hexagonal grids [3] and dividing the result by the average antenna radiation pattern.

The main advantages of the Neumann iteration, formulated in this way, is that it avoids large matrix products, it does not require to store huge matrices and it can be easily parallelized by computing each visibility sample $G[\Delta T^{dec}]$ separately. In the MIRAS case, having an Y-array with $N_T = 130$ antennas, 43 in each arm spaced $089\lambda$ and one at the center, the maximum vector size to be processed is $[N_T^2 \times 1] = [16.900 \times 1]$ and the size of the 2D-FFT is $[130 \times 130]$.

Depending on the magnitude of the errors and the number of antennas of the array (that affect $\Delta T_{noise}$ for the same integration time), convergence is usually achieved in up to 2 to 7 iterations for an Y-interferometer with 10 to 43 antennas per arm for the system tolerances of present MIRAS design and the available integration time [15]. Simulation results of this method are shown in the next section.

## 4. SIMULATION RESULTS

Figures 3 and 4 show two examples of the results obtained with the proposed inversion algorithm corresponding to the Mediterranean sea and the North of Europe brightness temperature scenes. Figures 3a and 4a show two computed L-band brightness temperature maps as they would appear from a 790 Km height satellite in a $98^\circ$ inclined sun-synchronous orbit [15]. In both cases antennas are assumed to be cup-dipoles [15] oriented in the along-track direction. It means that the brightness temperature that will be measured along the line $\xi = 0$ will be the vertical one, and, since the array is tilted, the brightness temperature that will be measured along the line $\eta = 0$, will be a linear combination of the vertical and the horizontal ones. Vertical and horizontal brightness temperatures are computed from the following physical parameters: soil and snow albedos, snow depth, soil roughness, vegetation albedos, soil moisture, soil surface temperature, ocean salinity, zonal and meridional winds over the oceans, vegetation height, ocean surface temperature and ocean ice cover. These parameters have

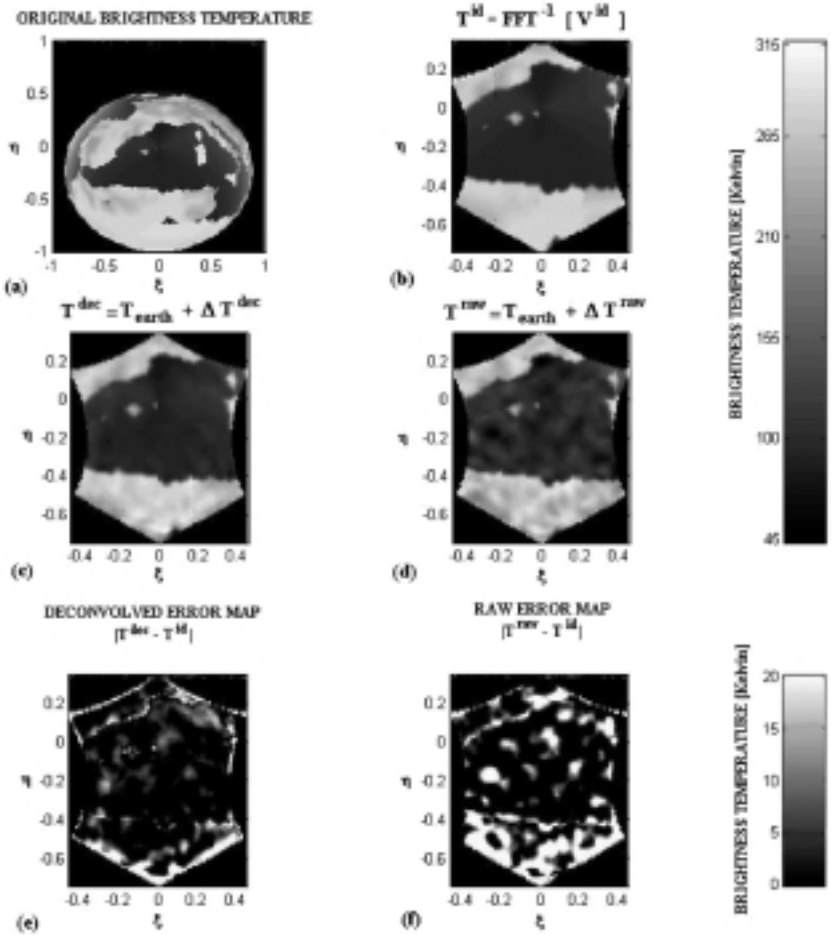


**Figure 3.** Mediterranean sea test scene: a) Original brightness temperature scene, b) Ideal brightness temperature scene in the alias-free FOV, c) Deconvolved brightness temperature in the alias-free FOV (7 iterations), d) Raw brightness temperature in the alias-free FOV, e) Error in the deconvolved brightness temperature map ( $\sigma^{dec} = 4.97$ K), f) Error in the raw brightness temperature map ( $\sigma^{raw} = 15.81$ K).

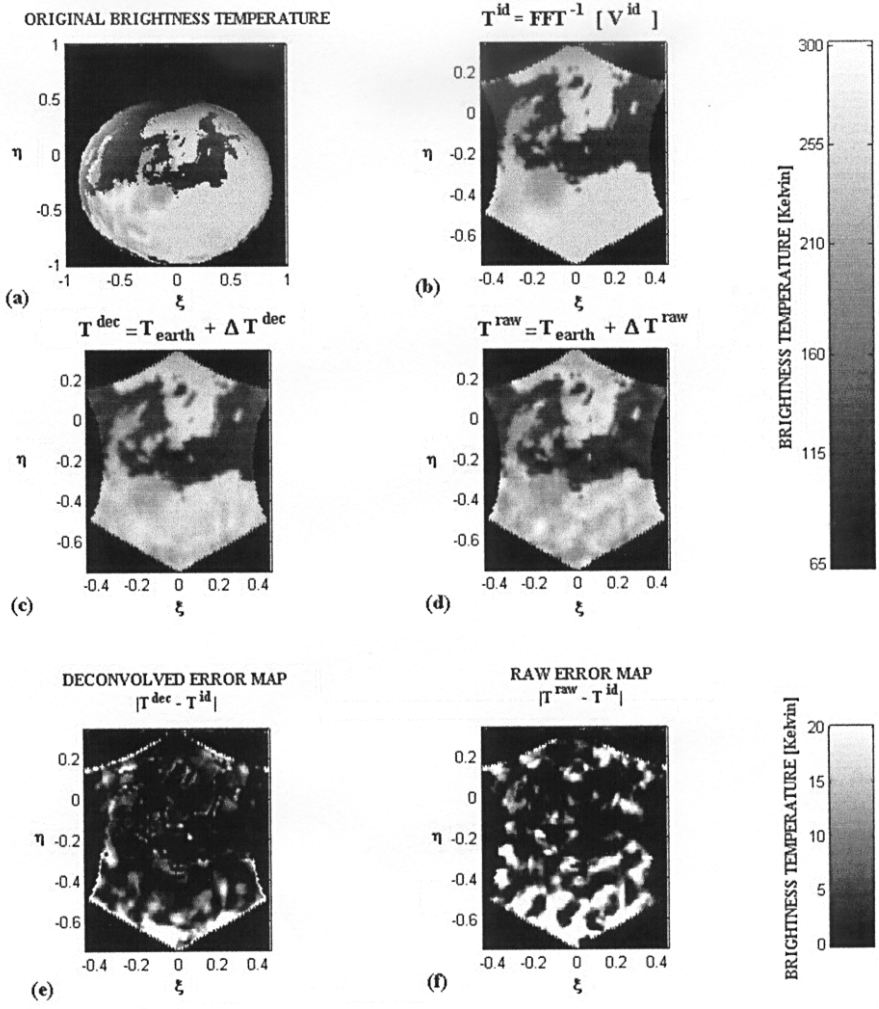


**Figure 4.** North Europe test scene: a) Original brightness temperature scene, b) Ideal brightness temperature scene in the alias-free FOV, c) Deconvolved brightness temperature in the alias-free FOV (4 iterations), d) Raw brightness temperature in the alias-free FOV, e) Error in the deconvolved brightness temperature map ( $\sigma^{dec} = 6.07$ K), f) Error in the raw brightness temperature map ( $\sigma^{raw} = 12.76$ K).

been extracted from the CD set [16, 17] and have been introduced in the brightness temperature models [18]. The data contained in these CD are mapped in a $1^\circ \times 1^\circ$ grid with a monthly temporal resolution (the data used corresponds to December 1988). This grid corresponds to a pixel's size of 110 Km $\times$ 110 Km over the Equator, which is larger than MIRAS' spot (30-50 Km). To overcome this problem, the loss of high frequency contents coming from the coast contrast, the computed brightness temperature pixels are interpolated bi-linearly and re-gridded to a thinner $1/12^\circ \times 1/12^\circ$ grid (9.26 Km $\times$ 9.26 Km) given by the NOAA ETOPOS 5 minutes resolution global digital elevation model.

Figures 3b and 4b show the alias-free FOV of the brightness temperature maps obtained by an hexagonal inverse Fourier transform [3] of the visibilities that would be measured by an ideal error-free interferometric radiometer of MIRAS size. Note the smoothing of the contours caused by the low-pass filtering due to the finite $(u, v)$ coverage. These images correspond to the maximum fidelity that can be achieved with the instrument and are used as a reference to test the proposed technique.

Figures 3d and 4d show the brightness temperature maps obtained from Equation 11, by means of a simple inverse Fourier transform and average antenna pattem compensation. The errors that can be appreciated in both images are mainly due to the large errors introduced in the antenna voltage pattems ( $10^\circ$ rms in phase and 10% in amplitude, a really worst case) for the computation of the visibility samples (Equation 1). Figures 3c and 4c show the brightness temperature maps that are recovered after 7 and 4 iterations respectively, at which the stopping criterion (Equation 19) is reached. As it can be appreciated, image quality is improved: the large oscillations in Figures 3d and 4d have almost disappeared and contrasts are sharper.

Figures 3e–4e and 3f–4f show the deconvolved and raw error maps computed from the substraction of the deconvolved maps (Figures 3c and 4c) and the ideal ones (Figures 3b and 4b), and the substraction of the raw maps (Figures 3d and 4d) and the ideal ones, respectively. Note that, after the inversion process, errors are much smaller, being concentrated in the regions with high contrasts and in the border of the alias free field of view, due to the truncation of the tails of the alias that enter in the alias free FOV.

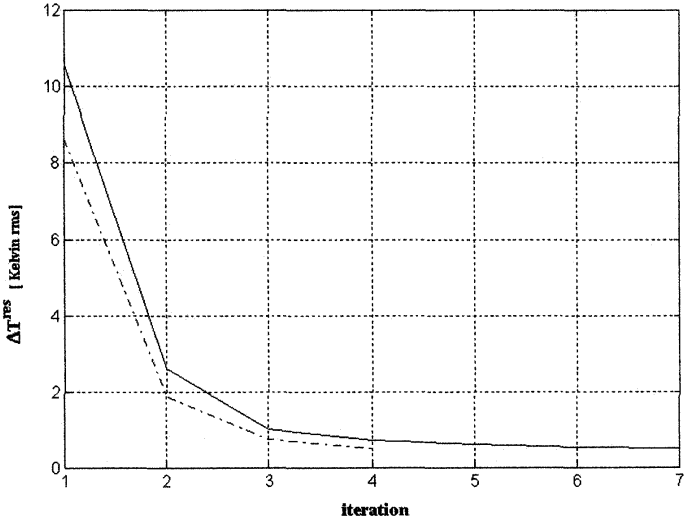


**Figure 5.** RMS value of the $\Delta T^{res(k)}$ terms added at each iteration (- Mediterranean test scene, - · - North Europe test scene)

Finally Figure 5 shows the rms value of the $\Delta T^{res(k)}$ terms (Equation 15) at each iteration. In the Mediterranean scene, the rms error computed in $\xi^2 + (\eta + 0.2)^2 \leq 0.2^2$ decreases from 15.81 K (Fig. 3d) down to 4.97 K (Fig. 3c) after 7 iterations, while in the North Europe scene, it decreases from 12.76 K (Fig. 4d) to 6.07 K (Fig. 4c) after 4 iterations. These remaining errors are larger than the stopping bound (Equation 19), because of the large antenna pattern errors increase the $\Delta T_{Gibbs}$ term due to the distortion of the aliases' shape. These simulations have been performed on a 100 MHz Pentium based personal computer. The associated computational load is about 80 Gflops to simulate the system and compute the set of corrupted visibility samples (Equation 1) and about 20 Gflops per iteration (Equations 6–19).

## 5. CONCLUSIONS

This work proposes an extension of the CLEAN algorithm suitable to two-dimensional large interferometric radiometers devoted to Earth observation. Its main advantages are. i) It is well suited to extended sources of thermal radiation. ii) The introduction of "a priori" information allows the processing of the set of differential visibility samples

which increases the alias-free FOV and boosts convergence speed. iii) It deals with uncalibrated instrument imperfections, mainly receiver frequency responses and antenna voltage pattem phase and amplitude mismatches. Since the solution is found by an iterative procedure, system drifts can be updated at each measurement without computational overhead. In addition, the use of hexagonal FFTs [3] reduces memory requirements, avoiding interpolations, signal-to-noise degradation and other induced artifacts.

## ACKNOWLEDGMENT

This work has been supported by the European Space Agency ESA, (within the framework of ESA MIRAS CCN 2 activities, with MATRA MARCONI SPACE as main contractor) and by the Spanish Ministry of Education and Culture CICYT TIC 96/0879.

## APPENDIX 1. CONVERGENCE OF THE NEUMANN INVERSION

Using Equations 15 to 19, the values of the residue and deconvolved temperature at the $k^{th}$ iteration can be expressed as

$$\Delta T^{res(k)} = (I - H)^k \Delta T^{raw} \tag{A1.1}$$

$$\Delta T^{dec(k)} = \sum_{n=0}^{k-1} (I - H)^n \Delta T^{raw} \tag{A1.2}$$

The matrix series of Equation A1.2, if it converges, tends to

$$\sum_{n=0}^{k-1} (I - H)^n \rightarrow H^{-1} \tag{A1.3}$$

provided that $|\lambda' - 1|_{max} < 1$, where $\lambda'$ are the eigenvalues of $H$. The residue given by Equation A1.1 shows the rms error committed, except for the $AF$ tails truncation. The eigenvalues of $H$ do not need to be computed since, in the case the process is not convergent, the norm of the residue vector grows at each iteration. In this case, a damping factor $\gamma < 1$ can be found to stabilize the process, as it is done in the standard CLEAN algorithm

$$\Delta T^{res(k)} = (I - \gamma H)^k \Delta T^{raw} \tag{A1.4}$$

$$\Delta T^{dec(k)} = \gamma \sum_{n=0}^{k-1} (I - \gamma H)^n \Delta T^{res(0)} \rightarrow H^{-1} \Delta T^{raw} \qquad \text{(A1.5)}$$

This resort is only necessary for very large antenna pattem errors, a situation which has not been found in simulations with real antenna pattems [15].

## REFERENCES


1. Mersereau, R. M., "The Processing of Hexagonally Sampled Signals", *Proceedings of the IEEE*, Vol. 67, No. 6, 930–949, June 1979.
2. Camps, A., J. Bará, I. Corbella, and F. Torres, "Visibility Inversion Algorithms over Hexagonal Sampling Grids", *Soil Moisture and Ocean Salinity Measurements and Radiometer Techniques*, WPP-87 109–114, ESA-ESTEC, Noordwijk, The Netherlands, April 20–22, 1995,
3. Camps, A., J. Bará, I. Corbella, and F. Torres, "The Processing of Hexagonally Sampled Signals with Standard Rectangular Techniques: Application to Aperture Synthesis Interferometer Radiometer", *IEEE Transactions on Geosc. and Remote Sensing*, Vol. 35, No. 1, 183–190, January 97.
4. Camps, A., *Application of Interferometric Radiometry to Earth Observation*, Ph.D. Thesis, Polytechnic University of Catalonia, Barcelona, Spain, November 1996.
5. Bará, J., A. Camps, and I. Corbella, "Bi-dimensional Discrete Formulation for Aperture Syntesis Radiometers", CNN 2 to Work Order No. 10 to ESTEC Contract No. 9777/92/PB.
6. Högborn, J. A., "Aperture synthesis with non-regular distribution of interferometer baselines", *Astron. Astrophys. Suppl.*, Vol. l5, 417–426, 1974.
7. Thompson, A. R., J. M. Moran, and G. W. Swenson, *Interferometry and Synthesis in Radio Astronomy*, John Wiley & Sons 1986.
8. *Synthesis Imaging in Radio Astronomy*, Vol. 6. NRAO Synthesis Imaging Summer School. Astronomical Society of the Pacific l989.
9. Torres, F., A. Camps, J. Bará, I. Corbella, and R. Ferrero, "Onboard Phase and Module Calibration of Large Aperture Synthesis Radiometers. Study Applied to MIRAS", *IEEE Transactions on Geoscience and Remote Sensing*, Vol. 34, No. 4, 1000–1009, July 96.

10. Camps, A., J. Bará, I. Corbella, and F. Torres, "Impact of Antenna Errors on the Radiometric Resolution of Large 2D Aperture Synthesis Radiometers: Study Applied to MIRAS", *Radio Science*, Vol. 32, No. 2, 657–668, March-April 1997.
11. Ruf, C. S., C. T. Swift, A. B. Tanner, and D. M. LeVine, "Interferometric Synthetic Aperture Radiometry for the Remote Sensing of the Earth", *IEEE Transactions on Geoscience and Remote Sensing*, Vol. 26, No.. 5, 597–611, September 1988.
12. Le Vine, D., M. Kao, A. Tanner, C. Swift, and A. Griffs, "Initial Results in the Development of a Synthetic Aperture Microwave Radiometer", *IEEE Trans. on Geoscience and Remote Sensing*, Vol. 28, No. 4, 614–619, July 1, 990.
13. Catedra, M. F., R. P. Torres, J. Basterrechea, and E. Gago, eds., *The CG-FT Method. Application of Signal Processing Techniques to Electromagnetics*, Artech House, 1995.
14. LeVine, D. M., "The Sensitivity of Synthetic Aperture Radiometers for Remote Sensing from Space", *Radio Science*, Vol. 25, No. 4, 441–453, July-August l990.
15. Matra Marconi Space, "MIRAS: Microwave Imaging Radiometer with Aperture Synthesis. Microwave Radiometry Critical Technical Development", *ESA-ESTEC, Final Report*, January 1995. ESTEC Contract 9777/92/NL/PB.
16. Meeson, B. W., F. E. Corprew, J. M. P. McManus, D. M. Myers, J. W. Closs, K. J. Sun, D. J. Sunday, P. J. Sellers, *1995 ISLSCP Initiative I-Global Data Sets for Land-Atmosphere Models*, 1987–1988, Volumes 1–5. Published on CD by NASA (USA_NASA_GDAAC_ISLSCP_00l-USA_NASA_GDAAC_ISLSCP_005).
17. Sellers, P. J., B. W. Meeson, J. Closs, J. Collatz, F. Corprew, D. Dazlich, F. G. Hall, Y. Kerr, R. Koster, S. Los, K. Mitchell, J. McManus, D. Myers, K. J. Sun, and P. Try, 1995. *An Overview of the ISLSCP Initiative I-Global Data Sets. On: ISLSCP Initiative I-Global Data Sets for Land-Atmosphere Models*, 1987-1988. Volume 1–5. Published on CD by NASA. Volume 1: USA_NASA_GDAAC_ISLSCP_00I, OVERVIEW.DOC
18. Fawwaz, T., R. Ulaby., K. Moore, and A. K. Fung, *Microwave Remote Sensing. Active and Passive Vols. II and III. Radar Remote Sensing and Surface Scattering and Emission Theory*, Artech House, 1982 and 1986.